LANGMUIR

Article

pubs.acs.org/Langmuir

Tracking Single DNA Nanodevices in Hierarchically Meso-Macroporous Antimony-Doped Tin Oxide Demonstrates Finite Confinement

Daniel Mieritz,[†] Xiang Li,[§] Alex Volosin,[†] Minghui Liu,[†,‡] Hao Yan,[†,‡] Nils G. Walter,[*,§] and Dong-Kyun Seo[*,†]

[†]School of Molecular Sciences and [‡]Center for Molecular Design and Biomimetics, Biodesign Institute and School of Molecular Sciences, Arizona State University, Tempe, Arizona 85287, United States

[§]Department of Chemistry, Single Molecule Analysis Group, University of Michigan, Ann Arbor, Michigan 48109-1055, United States

Supporting Information

ABSTRACT: Housing bio-nano guest devices based on DNA nanostructures within porous, conducting, inorganic host materials promise valuable applications in solar energy conversion, chemical catalysis, and analyte sensing. Herein, we report a single-template synthetic development of hierarchically porous, transparent conductive metal oxide coatings whose pores are freely accessible by large biomacromolecules. Their hierarchal pore structure is bimodal with a larger number of closely packed open macropores (~200 nm) at the higher rank and with the remaining space being filled with a gel network of antimony-doped tin oxide (ATO) nanoparticles that is highly porous with a broad size range of textual pores mainly from 20−100 nm at the lower rank. The employed carbon black template not only creates the large open macropores but also retains the highly structured gel network as holey pore walls. Single molecule fluorescence microscopic studies with fluorophore-labeled DNA nanotweezers reveal a detailed view of multimodal diffusion dynamics of the biomacromolecules inside the hierarchically porous structure. Two diffusion constants were parsed from trajectory analyses that were attributed to free diffusion (diffusion constant D = 2.2 $\mu m^2/s$) and to diffusion within an average confinement length of 210 nm (D = 0.12 $\mu m^2/s$), consistent with the average macropore size of the coating. Despite its holey nature, the ATO gel network acts as an efficient barrier to the diffusion of the DNA nanostructures, which is strongly indicative of physical interactions between the molecules and the pore nanostructure.

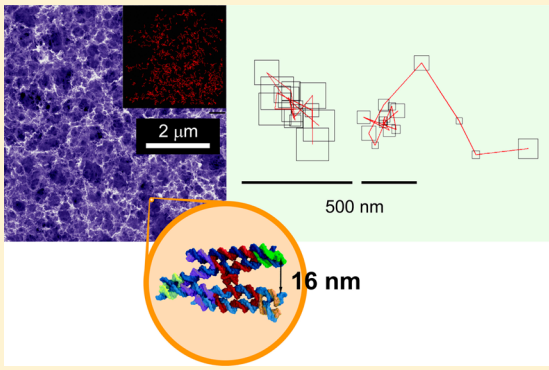

INTRODUCTION

Porous transparent conducting oxide (TCO) materials have recently emerged as high surface area electrodes that can host and provide an electronic conduit to biomacromolecules for harnessing their photoelectrochemical properties outside a cellular environment.[1−8] Extensive studies have been reported that utilized mesoporous materials (pore with = 2−50 nm) for small proteins in photosynthetic solar energy conversion[9−11] or in biosensors.[12,13] However, mesoporous materials are less than ideal for large biomacromolecules since their relatively small pore sizes are expected to impede diffusion of the particles, thus significantly reducing the ability to load them into the material. Indeed, it has been shown that biomacromolecules diffuse much more slowly as their size becomes comparable to that of the pore width.[14,15] By contrast, materials with macropores (pore width >50 nm) of three-dimensional connectivity enable more effective diffusion for large molecules,[3,14,16−20] but the available surface area is much smaller than offered by mesoporous materials.

Hierarchically porous materials exhibiting both macropores and mesopores have become popular recently based on their promise to overcome the disadvantages inherent to unimodal either mesoporous or macroporous materials, by offering macropores that facilitate long-range diffusion of large guest particles, while also containing mesopores connected to the macropores that expand the surface area available for adsorption of biomacromolecules.[21] Various studies have reported the synthesis of hierarchically porous oxide materials mainly of silica, titania,[21,22] and zirconia[21,23,24] and, to a lesser extent, of other metal oxides.[21,24−27] Our own recent studies have shown that functional cytochrome C (cyt C)−photoreaction center protein complexes from purple bacteria can be efficiently deposited on the pore surface of hierarchically porous ATO to yield a high photocurrent upon light exposure, although detailed information on the synthetic procedures and

Received: March 6, 2017
Revised: June 2, 2017
Published: June 2, 2017

DOI: 10.1021/acs.langmuir.7b00761
Langmuir 2017, 33, 6410−6418

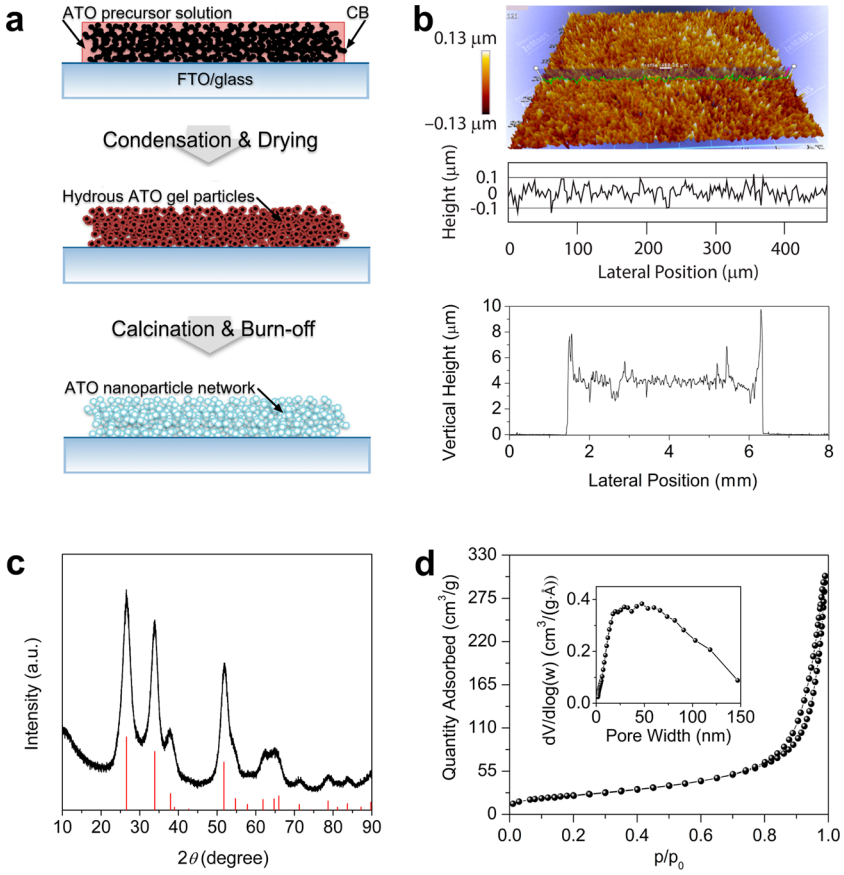

Figure 1. Characterizing the hierarchically meso-macroporous ATO coatings produced here. (a) Schematic diagram of the synthetic procedure for the fabrication of hierarchically porous ATO coatings. (b) Profilometry measurements on the hierarchically porous ATO coatings, taken by optical (top) and stylus profilometers (bottom). (c) PXRD pattern of hierarchically porous ATO; the red lines show the simulated peaks of the previously synthesized ATO with 6.2 atom % antimony doping (PDF # 01-075-2894). (d) Nitrogen sorption isotherms and (inset) BJH pore size distribution for the hierarchically porous ATO.

structural characteristics of the ATO coatings were not reported.[8]

Despite the increasing application of TCO materials as an effective host for biomacromolecules, however, it has not been understood how their hierarchical pore structure physically interacts with biomacromolecules as a characteristic critical for designing "smart" hybrid materials. As shown in previous studies of mesoporous materials,[15,28−30] single particle tracking (SPT) can provide a detailed view of the diffusion dynamics of guest molecules inside the porous host and thus yields unprecedented insights into the interactions of host and guest. Furthermore, an advantage of SPT is that the fluorescent particles directly map the landscape of the inner pore system of the host.[15] Herein we report the synthesis and detailed characterization of highly uniform, hierarchically porous ATO coatings via a newly developed carbon black template method. Using SPT of fluorophore-labeled DNA nanotweezers probes, we observe bimodal diffusion of guest biomacromolecules in the material. One diffusion regime corresponds to free diffusion in the large macropores while the other can be understood by significantly confined diffusion within the smaller macropores, limited by physical interaction with the gel-like mesoporous walls.

■ EXPERIMENTAL SECTION

Fabrication of Meso-Macroporous ATO Coatings. Details of the fabrication are described in the Supporting Information, with reference to the previous literature.[8]

Single Particle Tracking (SPT). For single molecule fluorescence imaging to perform SPT, previously reported DNA nanotweezers with Cy3 and Cy5 modifications[31] was utilized as a fluorescent reporter to probe the hierarchically porous ATO coating by single fluorescent particle tracking. The DNA nanotweezers (Figure S4; assembly reported in Supporting Information) were diluted to 200 pM into a final buffer of 1 × PBS supplemented with 10% (w/v) PEG 8000 and 1 mM $MgCl_2$ as the infiltration solution. A 40 μL infiltration solution was placed on top of an ATO coating and soaked at room temperature for 1 h to maximize adsorption. After deposition, the remaining solution was removed by airflow, and the ATO coating was washed twice with 40 μL imaging solution, composed of infiltration buffer supplemented with oxygen scavenger system, consisting of either 2.5 mM 3,4-dihydroxybenzoate, 25 nM protocatechuate dioxygenase, and 1 mM Trolox for imaging the nanotweezers probes or 0.63 mM 3,4-dihydroxybenzoate, 6.3 nM protocatechuate dioxygenase, and 0.25 mM Trolox for photobleaching experiments. Finally, a 20 μL imaging solution was deposited onto the ATO coating, and an mPEG-5000 (Laysan Bio, Inc.) coated glass slide was placed on top of the ATO coating and image solution. Before imaging, the sample was sealed with wax to prevent oxygen leaking into the imaging solution.

Three types of measurements were carried out. First, for observation of immobile DNA nanotweezers inside the ATO coating, a 40 μL infiltration solution containing 200 pM DNA nanotweezers was deposited on the coating for 1 h, followed by washing with

DOI: 10.1021/acs.langmuir.7b00761
Langmuir 2017, 33, 6410−6418

imaging solution twice before finally imaging in 20 μL imaging solution. Movies of 70−80 frames were collected along the z-axis throughout the coating at a rate of 500 ms/frame and a z-step size of 0.2 μm/frame. DNA nanotweezers were deposited and imaged along the z-axis at different Mg^{2+} concentrations of 1, 10, or 100 mM to study the effect of Mg^{2+} on immobilization. Second, for studying mobile DNA nanotweezers inside the ATO coating by single fluorescent particle tracking, a prebleaching process[30] was first carried out under 640 nm illumination to maximally photobleach the immobile probes, followed by taking movies of 1000 frames with a rate of 20 ms/frame. Third, for studying the aggregation status of probes inside the ATO coating, a photobleaching experiment was performed with the oxygen scavenger system concentration reduced to 25% during sample preparation (for faster bleaching). Movies of 300 frames were recorded at a rate of 150 ms/frame at a fixed image plane until all DNA nanotweezers were bleached.

SPT Data Analysis. For the analysis of all SPT data, custom MATLAB codes were combined with several established codes. For analyzing adsorbed DNA nanotweezers, the fluorescence signals of individual probes from different focal planes were first fitted and located by ImageJ with the QuickPALM plugin. The identified probes were further analyzed by a custom MATLAB code to calculate their z-position and 3D distribution. For the SPT of mobile fluorescent probes within the ATO coating, a previously reported MATLAB code[30] was applied to, first, locate probes by 2D Gaussian function fitting and to, second, track the trajectories of probes by fitting the same probe as identified by its spatial proximity over consecutive images until it diffused out of the focal plane. To ensure the accuracy of this analysis, tracks with at least five movement steps were analyzed, and only the first half of all data points were used for a diffusion coefficient calculation. A two-term cumulative probability distribution (CPD) function using a 2D motion model was applied to fit the trajectories of individual DNA nanotweezers and bin them into two subgroups based on differential diffusion speeds. A 2D diffusion is described as

$$P_{2D}(U, \tau) = 1 - e^{-U/(r^2(\tau))} \quad (1)$$

where $P_{2D}(U,\tau)$ is the probability of observing a squared displacement $r^2(\tau)$ value no larger than some value U during time τ.[32] Motion modes with different diffusion coefficients were defined by expanding eq 1 to include multiple fractions. We found the data from diffusing DNA nanotweezers to be best described by a two-term expansion with each a fast and a slow mobile mode, given as

$$P_{2D}(U, \tau) = \alpha(1 - e^{-U/(r^2(\tau))}) + (1 - \alpha)(1 - e^{-U/(r^2(\tau))}) \quad (2)$$

Here, α represents the fraction of the faster diffusion mode (term 1) whereas $1 - \alpha$ represents the fraction of the slower diffusion mode (term 2) due to confinement by and interactions with the enclosing matrix. Chosen to represent tracks that contain one, three, and five steps, the respective τ values of 0.020, 0.060, and 0.100 s were used in fitting the tracking data with eq 2. Based on the fitting result, mean-squared displacement (MSD) versus τ was plotted (Figure S8). The two diffusion coefficients and the corresponding fractions of time were then calculated from the plot. The pore size of the confining matrix was estimated from a diffusion model for restricted particle motion within a square:

$$\mathrm{MSD}(\tau) = \frac{L^2}{3}(1 - e^{-12D_0\tau/L^2}) \quad (3)$$

where D_0 is the initial diffusion constant and L is the length of the square.[32,33] Finally, for the photobleaching data analysis a custom LabView program was used to extract time traces of DNA nanotweezers from the recorded movies, which were further analyzed in the program QuB[34] to identify the number of photobleaching steps.

RESULTS AND DISCUSSION

Fabrication and Characterization of Meso-Macroporous ATO and Coatings Thereof. The overall synthetic strategy for producing hierarchically porous ATO coatings is depicted in Figure 1a. Briefly, a highly viscous mixture of an ATO precursor solution (red colored part in Figure 1a) and carbon black template particles (black particles) was doctor-bladed onto a glass substrate and then dried and calcined to yield the final product. The viscous mixture was prepared by high-shear mixing of a preprepared ATO precursor solution and a dispersion of carbon black particles. High-shear mixing was necessary because of the high viscosity of the dispersion. The initial dispersion contained 5 wt % carbon black, a sufficient amount to reach the percolation threshold as the solvent evaporates so that the carbon aggregates are in contact with each other throughout the entire volume of the final mixture.[35,36] We found that the carbon black was so hydrophobic that it would not disperse in water without copresence of PEG. 10 wt % PEG could provide a homogeneous stable dispersion of the carbon black, although we did not investigate in detail the effect of the PEG amount on the stability.

Subsequently, keeping the ATO precursor/carbon black mixture at room temperature for an hour led to ATO gel formation in the doctor-bladed coating.[37] After drying and calcination, the product was obtained as a semitransparent white coating well adhering to the FTO glass. The thickness and roughness of the final coatings were characterized by both optical and stylus profilometry methods (Figure 1b). Optical profilometry (top) allowed measurements of the height variations of the surface of the ATO coating. The largest peak-to-valley difference was less than 200 nm, attributed to the macropores exposed at the surface (see below). Optical profilometry was not successful, however, in determining the overall thickness of the coating due to the highly reflective glass substrate. Instead, stylus profilometry (Figure 1b, bottom) revealed that the coatings have a thickness of roughly 4 μm, except for ∼200 μm wide regions at the edges where the coating is 8−10 μm thick. Thicker ATO coating at the edges is due to surface tension of the solvents in the reaction mixture, tending to form a meniscus against the tape. Alternatively, an edge-on SEM image of the coating (Figure S1) shows that the thickness is 4.6 μm. The discrepancy in the thickness from the stylus profilometry and SEM may be due to the fact that the stylus damages the ATO coating surface during measurement, as evidenced from SEM images of the measured coatings (not shown).

The PXRD pattern of the ATO coatings (Figure 1c) shows that the crystal structure is rutile type with lattice constants a = 4.730 Å and c = 3.212 Å. The estimated crystallite size of the ATO is 3.5 nm from the Scherrer equation. It is noted that other known sol−gel techniques have produced larger particles, while epoxide-based sol−gel methods[38,39] or those using large amounts of multiblock copolymer surfactants[40] can produce nanoparticles small enough to generate similarly broad Bragg peaks. Figure 1d shows the results of nitrogen sorption studies, including the sorption isotherms and the resulting BJH pore size distribution. The BET surface area is measured to be 92 m^2/g and the accumulated pore volume 0.43 cm^3/g for the pore widths from 2 to 110 nm. The surface area and measured pore volume are larger for our ATO coating material than those for previously reported porous ATO prepared under similar

DOI: 10.1021/acs.langmuir.7b00761
Langmuir 2017, 33, 6410−6418

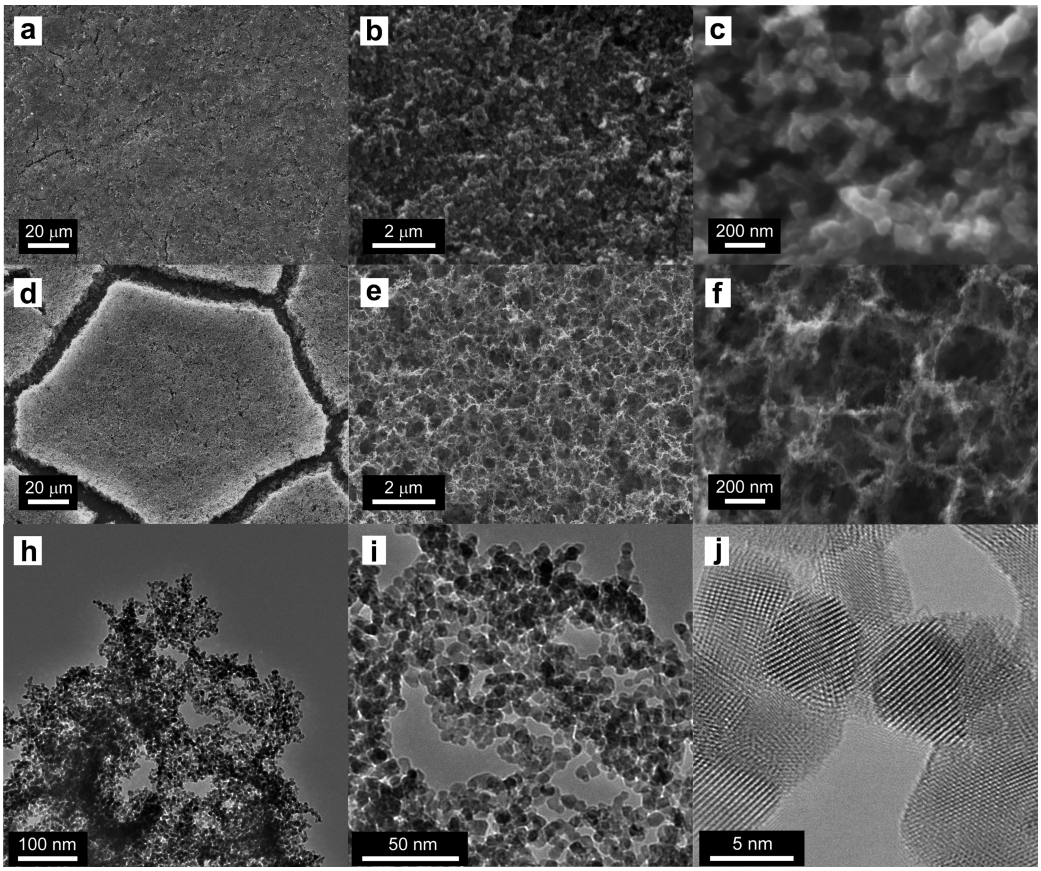

Figure 2. SEM micrographs of the template system; SEM and TEM micrographs of the coating (a–c, scale bars = 20 μm, 2 μm, and 500 nm, respectively). Carbon black/PEG template (d–f, scale bars = 20 μm, 2 μm, and 200 nm, respectively) and hierarchically porous ATO coating; (h) and (i) are TEM micrographs, and (j) is an HR-TEM micrograph of the hierarchically porous ATO; scale bars = 100, 50, and 5 nm, respectively.

synthetic conditions but without carbon black template.[37,41] The surface area corresponds to a spherical particle size of 9.3 nm, assuming the density of ATO is 7.02 g/cm^3.[41] This particle size is considerably larger than the one of 3.5 nm estimated from the Scherrer equation, which suggests that the particles are sintered well,[37] which is critical for conductive and mechanically robust coatings.

In Figure 1d, both the adsorption and desorption isotherms exhibit a type III[42] shape with a lack of saturation, indicating the presence of macropores. The coexistence of mesopores is evident from the hysteresis loop in the isotherms, and the H5-type loop indicates that mesopores are relatively large and well-connected.[43] The BJH pore size distribution from the desorption isotherm is shown in the inset of Figure 1d where a broad distribution of the pore sizes is observed spanning both mesopores and macropores mainly from 20 to 100 nm with a broad maximum peak around 50 nm. Macropores are also observed in the range over >150 nm, but the BJH analysis does not provide a meaningful information in that region. While mercury intrusion porosimetry was more suitable for such large pores, the technique was not employed in our studies because the highly porous gel structure of the ATO material was too fragile to withstand the high operating pressure (>40 atm) required for this pore size range.

Interpreting How the Template System Translates to Pore Structure and Studying the Meso-Macropore Characteristics of ATO with SEM and TEM. Figure 2 shows SEM images of a carbon black template coating prepared without the ATO precursors (a–c) and an ATO coating product (d–f). The carbon black template coating shows a uniform coverage of the glass substrate (a, b) with some small cracks caused by drying and shrinkage. A closer look shows carbon black aggregates of 100–500 nm in size that are loosely packed (Figure 2c). Meanwhile, the ATO coating in Figure 2d shows shrinkage of the coating probably during drying and subsequent formation of ∼10 μm wide cracks. Although the extent of shrinkage is difficult to quantify, a linear shrinkage of ∼20% is consistent with the studies from other methods such as polymer bead templating.[3,17] Despite the shrinkage, the coating maintains its good contact with the underlying glass substrate. The surface of the ATO coating (Figure 2e) features macropores with pore widths ranging from 100 to 400 nm at the surface. The macropores are closely packed but separated by walls having a thickness of 30–50 nm. When compared to Figure 2b, it is clear that the macroporosity observed in Figure 2e is a result of the sacrificial carbon black template because the macropore size and distribution roughly matches those of the template. Considering that the pore structure in the ATO coating is a negative replica of the carbon black template, it is reasonable to assume that these macropores are well connected with each other, providing highly open windows for molecules to diffuse through. In addition, the macropore walls are highly textured, which indicates that the walls themselves are further nanostructured (Figure 2f).

For examination of the nanostructures of the ATO products, representative TEM and HR-TEM images of the hierarchically porous ATO structure are shown in Figure 2g–i. Figure 2g shows a structure with large pores (>100 nm) surrounded by

DOI: 10.1021/acs.langmuir.7b00761
Langmuir 2017, 33, 6410–6418

nanoparticles that are strongly aggregated and fused together (h and i). In Figure 2g, the 3D nature of the pore structure is still not clear because of the limitation of TEM images as a 2D projection of a 3D structure, but the large pores appear to be well connected. The HR-TEM image in Figure 2i shows that the nanoparticles are strongly fused and that their size is around 4 nm, in agreement with the Scherrer analysis results. Observation of lattice fringes confirms the high crystallinity of the nanoparticles.

It emerges from these analyses that the ATO coatings have a bimodal hierarchical pore structure, with a larger number of closely packed open macropores (~200 nm) at the higher rank and the remaining space filled with a gel network of ATO nanoparticles that is highly porous with a broad size range of textual pores mainly from 20 to 100 nm at the lower rank. The effect of the carbon black template on formation of the ATO nanoparticle networks can be examined by comparing the microscopic structures of the ATO product with those of the carbon black template itself (Figure S2) and with those of the ATO/carbon black composite (Figure S3). The latter was prepared by following the same synthetic condition but by calcining in an inert N_2 gas flow instead to leave the carbon black intact in the structure. The carbon black template consists of open-structure aggregates (100−300 nm) that are assembled from primary carbon particles (20−50 nm). TEM images of the ATO/carbon black composite (Figure S3) show that the carbon black particles are decorated with much smaller ATO nanoparticles (4−10 nm). However, the ATO nanoparticles cover the carbon black particles only sparsely so that the resulting ATO networks are expected to be very open and porous once the carbon black particles are burned off. Therefore, the role of the carbon back template is the creation not only of the large open macropores but also of the highly structured gel network of holey pore walls.

SPT Studies. For SPT, fluorophore-labeled DNA nanotweezers were used as a well-characterized probe.[31,44] The DNA nanotweezers are composed of two arms with a spacing duplex (Figure S4b). Each arm is ~14 nm in length, and the distance of the ends of the two arms in the "open" conformation is ~16 nm,[31] resulting in a relatively large molecular size to probe the efficiency of entrance and diffusion through our ATO coatings. The DNA nanotweezers were modified with one Cy3 dye at the end of one arm and one Cy5 at the other. Because of the background in the Cy3 channel, the lower background Cy5 channel was generally chosen for SPT in the ATO film. The DNA probe solution was initially loaded into the ATO coating over 1 h for adsorption, followed by the sample preparation in Figure S4.

The prepared ATO coating sample was imaged first along the *z*-axis in the Cy5 channel to record the loading of immobile probes inside the coating (Movie S1, 500 ms exposure per frame). Figure 3a shows raw images of adsorbed DNA nanotweezers probes in three focal planes inside the ATO coating, with the corresponding spatial distribution summarized in Figure 3b. The fluorescent probes are observed over a range of ~7 μm in the *z*-direction, which is reasonably consistent with the thickness determined by both profilometry and edge-on SEM, given the localization error quantified by a control measurement of DNA nanotweezers deposited directly onto the coverslip, which shows a probe distribution over ~1 μm (Movie S2 and Figure S5). The distribution of DNA probes throughout the coating, with a higher density near the surface from where the deposition occurred (Figure 3b), indicates that

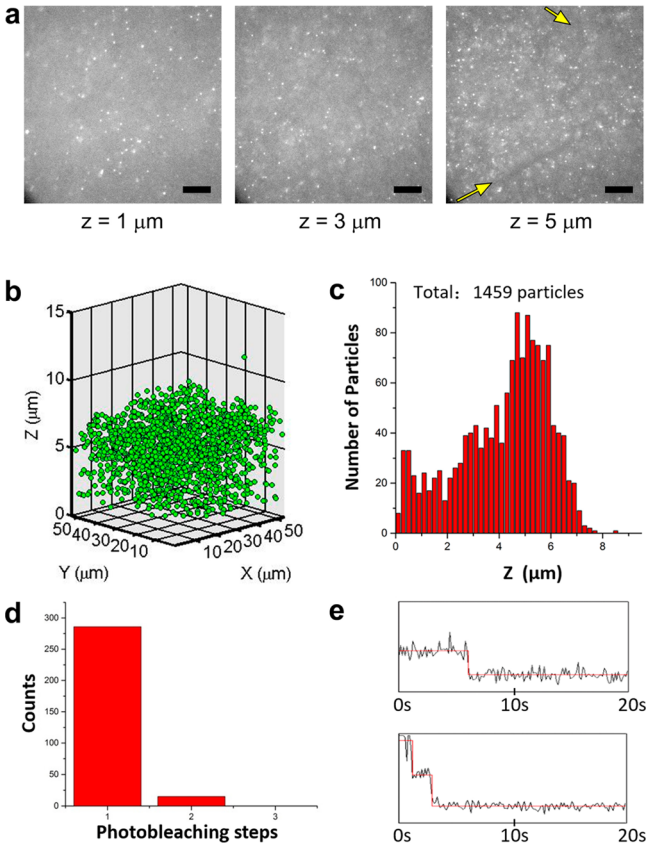

Figure 3. Distribution of adsorbed fluorescence nanotweezers along the *z*-axis inside the ATO coating, and photobleaching study. (a) Raw images of DNA nanotweezers at different focal planes; yellow arrows indicate where a crack enters and leaves the frame (scale bars = 5 μm). (b) Probe counting results are shown in 3D where green dots represent counts. (c) Histogram summarizing the counts at various *z*-axis heights. (d) Number of steps for photobleaching, and (e) representative traces of one-step (top) and two-step photobleaching (bottom).

the ATO coating is highly porous and accessible. We also found evidence for small cracks in the material, as outlined by a lack of adsorbed probes in the region whose two ends are indicated by yellow arrows (Figure 3a, z = 5 μm).

Studying Electrostatic Interactions between DNA and ATO Pore Walls. The effect of Mg^{2+} ions in the buffer solution on the suitability of the porous ATO as an effective host for DNA was studied by examining the DNA distributions in imaging solutions with two Mg^{2+} concentrations, 10 and 100 mM (Figure S6). From the distribution histograms (Figure 3c and Figure S5b,d), we found that the total amount of DNA remaining in the coatings after washing increased gradually as the Mg^{2+} concentration increases. In a separate experiment, the zeta potential of aqueous dispersions of scraped ATO coatings was shown to rapidly increase from −20 to 5 mV between 0 and 7.5 mM Mg^{2+} and then to level off (Figure S7), indicating that the ATO surface becomes positively charged upon adsorption of Mg^{2+} cations at Mg^{2+} concentrations above ~3 mM and thus can electrostatically attract negatively charged DNA. Interestingly, we observed that even at 1 mM Mg^{2+} (Figure 3b), a significant amount of DNA remains within the coating. The apparent presence of DNA at the low Mg^{2+} concentration may be due to the pore structure's impeding diffusion, although it is not possible to discount transient

DOI: 10.1021/acs.langmuir.7b00761
Langmuir 2017, 33, 6410−6418

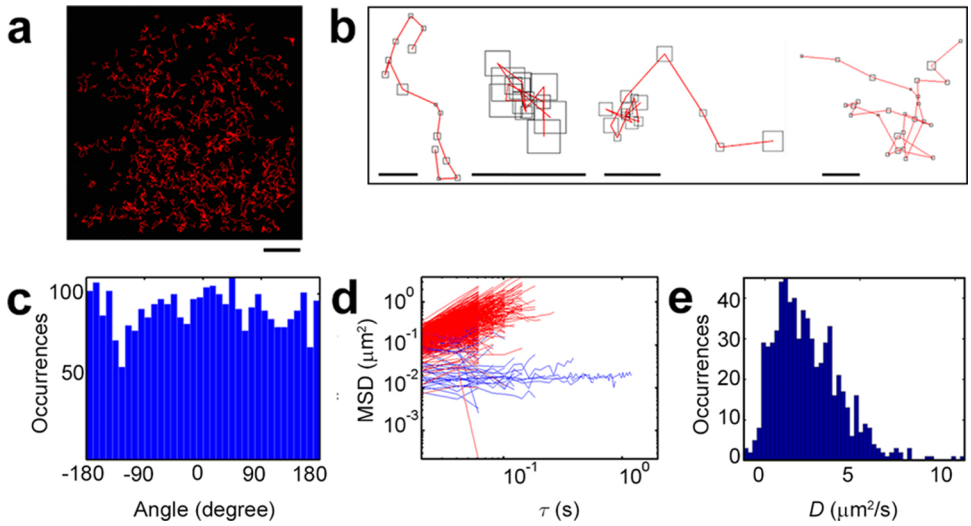

Figure 4. Diffusion behaviors of single DNA nanotweezers inside the ATO coating. (a) Raw image of diffusion paths from an entire field of view (leftmost, scale bar = 10 μm). (b) Exemplary single particle trajectories (scale bars = 500 nm). (c) Distribution of angles between successive diffusion steps. (d) Plot of MSD versus time lag, τ; the trajectories can be generally divided into two subgroups based on their slope: mobile (red) and confined (blue). (e) Distribution of apparent diffusion coefficients derived from the MSD plots.

binding of DNA in some areas of the ATO surface. A larger amount of DNA can stay in the coating at higher Mg^{2+} concentrations, supporting the presumption of Coulombic attraction between the negatively charged DNA and the Mg^{2+}-saturated, positively charged ATO surface. The increase in DNA nanotweezers adsorbed with increasing Mg^{2+} concentration was modest, which is in agreement with the gradual increase of the zeta potential in that high Mg^{2+} concentration region.

Studying Intermolecular Interactions within ATO Pores. Next, a photobleaching experiment was carried out to examine whether adsorbed DNA probes would inadvertently agglomerate inside the coating (Figure 3d and Movie S3), hence hampering proper diffusion kinetics studies. Such agglomeration can also deleteriously affect the functionality of biomacromolecules.[45,46] By analyzing the number of photobleaching steps as described (Figure 3e),[47] we found that the majority of DNA nanotweezers remain as single units without significant agglomeration. We conclude that our hierarchically porous ATO coatings provide an environment compatible with hosting individual DNA nanostructures.

Photobleaching was also necessary since the high background from adsorbed probes otherwise did not allow successful tracking of diffusing probes. After photobleaching, fresh probe molecules enter the bleached area, as detected under the microscope. Because of preadsorbed, now photobleached, DNA nanotweezers on the ATO surface in this area, the new molecules are expected to find fewer interaction spaces with the surface. Consistent with this notion, the new DNA nanotweezers showed fast and hence untraceable diffusion (Movie S3 and Movie S4). For successful SPT of the diffusing probes, their motion had to be slowed down sufficiently for detection, which we accomplished by introducing 10% (w/v) PEG into the buffer. Movies with 1000 frames at 20 ms/frame were recorded for subsequent SPT analysis (Movie S5).

Statistical Analysis of Single-Particle Trajectory Data. A representative field of view with observed tracks is shown in Figure 4a. The DNA probes appear to diffuse randomly, but a closer inspection reveals different types of individual diffusion trajectories (Figure 4b). Most of the trajectories behave like the Brownian diffusion expected in an open space (e.g., the far left and right ones in Figure 4b), while some traces indicate the tracked probes as temporarily confined (e.g., the second one from the left in Figure 4b). The confinement is not permanent (finite confinement) and some trajectories show free diffusion of the probe after a brief confinement (e.g., the second one from the right in Figure 4b).

To extract kinetic information, further track analyses were carried out using custom MATLAB codes.[30] In a given focal plane, 2D random walks were observed from an analysis of the distribution of angles between successive diffusion steps, as evident from the equal distribution of angles in each direction (Figure 4c). This result is expected since the observed 2D trajectories are projections of the 3D random motions of the probes inside the ATO coating. Moreover, most of the observed tracks had fewer than 10 steps, owing to the fast 3D diffusion in and out of the imaging plane, further supporting fast 3D random motion behavior.

The diffusion coefficients (D) of individual particles were calculated from the Einstein−Smoluchowski equation: $\mathrm{MSD}(\tau) = 2nD\tau$, where n is the dimensionality of motion, by plotting their mean-square displacement (MSD) versus the time lag (τ), with $n = 2$ in this case (Figure 4d). The DNA probes can be generally divided into two major groups based on the slopes of their linear fits, with red color used for average slopes >0.1 $\mu m^2/s$ (fast diffusion, Figure 4d) and blue color for average slopes $\leq$0.1 $\mu m^2/s$ (slow diffusion). The distribution of calculated diffusion coefficients is shown in Figure 4e, with a major peak around ~2 $\mu m^2/s$.

To further distinguish the motional modes of the DNA probes in the ATO coating, a CPD analysis was carried out by analyzing all probe trajectories together. A 2D random motion model was chosen for the CPD plot fitting with three τ value components: τ = 0.020, 0.060, and 0.100 s. The best fit was obtained with two diffusion coefficients (Figure S8), indicating that DNA nanotweezers spend ~85% of their time in a fast motion mode (red data points in Figure S8b) and ~15% of their time in a slow motion mode (green data points in Figure S8b). A model with only one diffusion coefficient resulted in a poor fit (Figure S9a), while three diffusion coefficients did not

DOI: 10.1021/acs.langmuir.7b00761
Langmuir 2017, 33, 6410−6418

improve the fitting in a meaningful way (Figure S9b). Of the two diffusion constants, the fast motion mode exhibited a linear relationship between MSD and τ, where $D = 2.2\ \mu m^2/s$ was calculated from the slope using the Einstein−Smoluchowski equation, accounting for all freely diffusing probes that were trackable. This value is a lower estimate of the free diffusion constant since the fastest moving probes likely blur given our limiting acquisition speed of 20 ms/frame.

The slow motion mode is inconsistent with free diffusion, since the corresponding MSD versus τ graph shows nonlinear behavior (the inset in Figure S8b).[32,33] This nonlinear behavior can be modeled either as a strong confinement mode with a (highly) impermeable boundary or as an obstacle-impeded diffusion mode.[33] In the latter case, free diffusion of a molecule is impeded by the presence of immobile obstacles to diffusion. Percolation theory indicates that long-range diffusion will cease altogether if the obstacles are immobile and cover more than a threshold fraction of the diffusion medium. While the rigid networks of ATO nanoparticles may act as immobile obstacles that percolate the body of the diffusion medium, the obstacle-impeded diffusion model does not explain the observed finite confinement of the probe molecules. By fitting our data with the confinement model as a first approximation eq 3, both the initial diffusion constant D_0 and the average side length L of confinement can be calculated, which yielded 0.12 $\mu m^2/s$ and ∼210 nm, respectively. This side length is consistent with the range of macropore sizes observed by SEM (Figure 2e,f), validating the confinement model for the observed slow diffusion mode. That is the mesoporous ATO walls provide an effective barrier to the DNA nanotweezers molecules whose diffusion is severely hindered in the macropores surrounded by the gel network walls, which have a diameter in the range of 200 nm. By contrast, the dominant fast diffusion mode implies that most of the macropores are open and connected with each other so that the biomacromolecules can diffuse in the free spaces between the mesoporous walls.

CONCLUSION

In summary, we have successfully fabricated hierarchically porous transparent conductive ATO coatings whose pores are freely accessible by biomacromolecules. Their hierarchal pore structure is bimodal with a larger number of closely packed open macropores (∼200 nm) at the higher rank and with the remaining space occupied by a gel network of ATO nanoparticles that is highly porous with a broad size range of textual pores mainly from 20 to 100 nm at the lower rank. The role of carbon black template is critical not only in creation of the large open macropores but also in formation of the highly structured gel network as holey pore walls. SPT studies with fluorophore-labeled DNA nanotweezers unveil a detailed view of the multimodal diffusion dynamics of biomacromolecules inside this hierarchically porous architecture. We find two diffusion regimes: one corresponding to free diffusion in the large macropores (diffusion constant $D = 2.2\ \mu m^2/s$) and the other reflecting partially confined diffusion within the macropores (∼200 nm) that are inhibited by the physical interaction with the gel network walls ($D = 0.12\ \mu m^2/s$). Overall, the hierarchically porous ATO coating is a promising substrate to incorporate large guest molecules such as DNA nanostructures while supporting their molecular integrity, monodispersity, and free diffusion.

ASSOCIATED CONTENT

Supporting Information

The Supporting Information is available free of charge on the ACS Publications website at DOI: 10.1021/acs.langmuir.7b00761.

Figures S1−S9, edge-on SEM image of meso-macroporous ATO coating; TEM micrographs of the carbon black template with and without pyrolized ATO precursor; details of the experimental design; control experiment; results of changing [Mg^{2+}] on the density of stationary DNA probes; plot of measured zeta potential of the ATO coating material at various [Mg^{2+}]; verification of the models employed to analyze CPD data; experimental details of coating fabrications; descriptions of characterizations; SPT study details (PDF)

Movie S1: immobile probes inside the coating (AVI)

Movie S2: immobile probes on the coverslip without ATO coating (AVI)

Movie S3: photobleaching experiment (AVI)

Movie S4: fast diffusion (without PEG) (AVI)

Movie S5: data for SPT analysis (AVI)

AUTHOR INFORMATION

Corresponding Authors

*E-mail: nwalter@umich.edu.

*E-mail: dseo@asu.edu.

ORCID

Hao Yan: 0000-0001-7397-9852

Dong-Kyun Seo: 0000-0001-9201-4079

Author Contributions

D.M. and X.L. contributed equally.

Notes

The authors declare no competing financial interest.

ACKNOWLEDGMENTS

The authors are grateful to Dr. Soma Dhakal and Dr. Yi Liao for their help in the single particle tracking analysis, Dr. Alexander Johnson-Buck and Dr. Laurie Heinicke for their assistance on the codes of immobile particles and photobleaching data analysis, and the Single Molecule Analysis in Real-Time (SMART) Center of the University of Michigan, seeded by NSF MRI-R2-ID Award DBI-0959823 to N.G.W. as well as Dr. Damon Hoff for training and technical advice on the Center's Single Particle Tracker microscope. This work was supported by Army Research Office MURI Award W911NF-12-1-0420 to N.G.W., H.Y., and D.-K.S. All parties reviewed and contributed to the manuscript.

ABBREVIATIONS

ATO, antimony-doped tin oxide; DNA, deoxyribonucleic acid; TCO, transparent conducting oxide; Cyt *c*, cytochrome *c*; SEM, scanning electron microscopy; PXRD, powder X-ray diffraction; SPT, single particle tracking; BET, Brunauer−Emmett−Teller; BJH, Barrett−Joyner−Halenda; PBS, phosphate-buffered saline; PEG, poly(ethylene glycol); FTO, fluorine-doped tin oxide; TEM, transmission electron microscopy; HR-TEM, high-resolution transmission electron microscopy; MSD, mean-square displacement; CPD, cumulative probability distribution.

DOI: 10.1021/acs.langmuir.7b00761
Langmuir 2017, 33, 6410−6418

REFERENCES

(1) Kwan, P.; Schmitt, D.; Volosin, A. M.; McIntosh, C. L.; Seo, D.-K.; Jones, A. K. Spectroelectrochemistry of cytochrome c and azurin immobilized in nanoporous antimony-doped tin oxide. *Chem. Commun.* **2011**, *47* (45), 12367−12369.

(2) Frasca, S.; Molero Milan, A.; Guiet, A.; Goebel, C.; Pérez-Caballero, F.; Stiba, K.; Leimkühler, S.; Fischer, A.; Wollenberger, U. Bioelectrocatalysis at mesoporous antimony doped tin oxide electrodes—Electrochemical characterization and direct enzyme communication. *Electrochim. Acta* **2013**, *110*, 172−180.

(3) Liu, Y.; Peters, K.; Mandlmeier, B.; Müller, A.; Fominykh, K.; Rathousky, J.; Scheu, C.; Fattakhova-Rohlfing, D. Macroporous indium tin oxide electrode layers as conducting substrates for immobilization of bulky electroactive guests. *Electrochim. Acta* **2014**, *140*, 108−115.

(4) Topoglidis, E.; Lutz, T.; Durrant, J. R.; Palomares, E. Interfacial electron transfer on cytochrome-c sensitised conformally coated mesoporous TiO_2 films. *Bioelectrochemistry* **2008**, *74* (1), 142−148.

(5) Topoglidis, E.; Astuti, Y.; Duriaux, F.; Grätzel, M.; Durrant, J. R. Direct Electrochemistry and Nitric Oxide Interaction of Heme Proteins Adsorbed on Nanocrystalline Tin Oxide Electrodes. *Langmuir* **2003**, *19* (17), 6894−6900.

(6) Topoglidis, E.; Cass, A. E. G.; O'Regan, B.; Durrant, J. R. Immobilisation and bioelectrochemistry of proteins on nanoporous TiO_2 and ZnO films. *J. Electroanal. Chem.* **2001**, *517* (1−2), 20−27.

(7) Müller, V.; Rathousky, J.; Fattakhova-Rohlfing, D. Covalent immobilization of redox protein within the mesopores of transparent conducting electrodes. *Electrochim. Acta* **2014**, *116*, 1−8.

(8) Carey, A.-M.; Zhang, H.; Mieritz, D.; Volosin, A.; Gardiner, A. T.; Cogdell, R. J.; Yan, H.; Seo, D.-K.; Lin, S.; Woodbury, N. W. Photocurrent Generation by Photosynthetic Purple Bacterial Reaction Centers Interfaced with a Porous Antimony-Doped Tin Oxide (ATO) Electrode. *ACS Appl. Mater. Interfaces* **2016**, *8* (38), 25104−25110.

(9) Maksimov, E. G.; Lukashev, E. P.; Seifullina, N. K.; Nizova, G. V.; Pashchenko, V. Z. Photophysical properties of hybrid complexes of quantum dots and reaction centers of purple photosynthetic bacteria Rhodobacter sphaeroides adsorbed on crystalline mesoporous TiO_2 films. *Nanotechnol. Russ.* **2013**, *8* (7), 423−431.

(10) Ravi, S. K.; Tan, S. C. Progress and perspectives in exploiting photosynthetic biomolecules for solar energy harnessing. *Energy Environ. Sci.* **2015**, *8* (9), 2551−2573.

(11) Jiang, N.; Yang, X.-Y.; Deng, Z.; Wang, L.; Hu, Z.-Y.; Tian, G.; Ying, G.-L.; Shen, L.; Zhang, M.-X.; Su, B.-L. A Stable, Reusable, and Highly Active Photosynthetic Bioreactor by Bio-Interfacing an Individual Cyanobacterium with a Mesoporous Bilayer Nanoshell. *Small* **2015**, *11* (17), 2003−2010.

(12) Etienne, M.; Zhang, L.; Vilà, N.; Walcarius, A. Mesoporous Materials-Based Electrochemical Enzymatic Biosensors. *Electroanalysis* **2015**, *27* (9), 2028−2054.

(13) Hasanzadeh, M.; Shadjou, N.; Eskandani, M.; Guardia, M. d. l. Mesoporous silica-based materials for use in electrochemical enzyme nanobiosensors. *TrAC, Trends Anal. Chem.* **2012**, *40*, 106−118.

(14) Hormann, K.; Tallarek, U. Mass transport properties of second-generation silica monoliths with mean mesopore size from 5 to 25 nm. *J. Chromatogr. A* **2014**, *1365*, 94−105.

(15) Zürner, A.; Kirstein, J.; Doblinger, M.; Brauchle, C.; Bein, T. Visualizing single-molecule diffusion in mesoporous materials. *Nature* **2007**, *450* (7170), 705−708.

(16) Arsenault, E.; Soheilnia, N.; Ozin, G. A. Periodic Macroporous Nanocrystalline Antimony-Doped Tin Oxide Electrode. *ACS Nano* **2011**, *5* (4), 2984−2988.

(17) Nandiyanto, A. B. D.; Suhendi, A.; Kisakibaru, Y.; Ogi, T.; Okuyama, K. Generation of Highly Ordered Porous Antimony-Doped Tin Oxide Film by A Simple Coating Method with Colloidal Template. *Int. J. Chem. Biol. Eng.* **2012**, *6* (1), 1142−1145.

(18) Tong, J.; Anderson, J. L. Partitioning and diffusion of proteins and linear polymers in polyacrylamide gels. *Biophys. J.* **1996**, *70* (3), 1505−13.

(19) Farnan, D.; Frey, D. D.; Horváth, C. Surface and pore diffusion in macroporous and gel-filled gigaporous stationary phases for protein chromatography. *J. Chromatogr. A* **2002**, *959* (1−2), 65−73.

(20) Lévesque, S. G.; Lim, R. M.; Shoichet, M. S. Macroporous interconnected dextran scaffolds of controlled porosity for tissue-engineering applications. *Biomaterials* **2005**, *26* (35), 7436−7446.

(21) Yuan, Z.-Y.; Su, B.-L. Insights into hierarchically meso-macroporous structured materials. *J. Mater. Chem.* **2006**, *16* (7), 663−677.

(22) Hwang, J.; Jo, C.; Hur, K.; Lim, J.; Kim, S.; Lee, J. Direct Access to Hierarchically Porous Inorganic Oxide Materials with Three-Dimensionally Interconnected Networks. *J. Am. Chem. Soc.* **2014**, *136* (45), 16066−16072.

(23) Reeder, D. H.; Carr, P. W.; Flickinger, M. C.; McCormick, A. V. Diffusion of Nonadsorbing Polymers within Hierarchically Structured Colloidal Aggregates. *J. Colloid Interface Sci.* **2000**, *226* (2), 277−285.

(24) Smått, J.-H.; Sayler, F. M.; Grano, A. J.; Bakker, M. G. Formation of Hierarchically Porous Metal Oxide and Metal Monoliths by Nanocasting into Silica Monoliths. *Adv. Eng. Mater.* **2012**, *14* (12), 1059−1073.

(25) Smått, J.-H.; Weidenthaler, C.; Rosenholm, J. B.; Lindén, M. Hierarchically Porous Metal Oxide Monoliths Prepared by the Nanocasting Route. *Chem. Mater.* **2006**, *18* (6), 1443−1450.

(26) Huang, S.-Z.; Jin, J.; Cai, Y.; Li, Y.; Deng, Z.; Zeng, J.-Y.; Liu, J.; Wang, C.; Hasan, T.; Su, B.-L. Three-Dimensional (3D) Bicontinuous Hierarchically Porous Mn_2O_3 Single Crystals for High Performance Lithium-Ion Batteries. *Sci. Rep.* **2015**, *5*, 14686.

(27) Davis, M.; Ramirez, D. A.; Hope-Weeks, L. J. Formation of Three-Dimensional Ordered Hierarchically Porous Metal Oxides via a Hybridized Epoxide Assisted/Colloidal Crystal Templating Approach. *ACS Appl. Mater. Interfaces* **2013**, *5* (16), 7786−7792.

(28) Skaug, M. J.; Schwartz, D. K. Tracking Nanoparticle Diffusion in Porous Filtration Media. *Ind. Eng. Chem. Res.* **2015**, *54* (16), 4414−4419.

(29) Kirstein, J.; Platschek, B.; Jung, C.; Brown, R.; Bein, T.; Brauchle, C. Exploration of nanostructured channel systems with single-molecule probes. *Nat. Mater.* **2007**, *6* (4), 303−310.

(30) Liao, Y.; Yang, S. K.; Koh, K.; Matzger, A. J.; Biteen, J. S. Heterogeneous Single-Molecule Diffusion in One-, Two-, and Three-Dimensional Microporous Coordination Polymers: Directional, Trapped, and Immobile Guests. *Nano Lett.* **2012**, *12* (6), 3080−3085.

(31) Dhakal, S.; Adendorff, M. R.; Liu, M.; Yan, H.; Bathe, M.; Walter, N. G. Rational design of DNA-actuated enzyme nanoreactors guided by single molecule analysis. *Nanoscale* **2016**, *8* (5), 3125−3137.

(32) Lommerse, P. H. M.; Blab, G. A.; Cognet, L.; Harms, G. S.; Snaar-Jagalska, B. E.; Spaink, H. P.; Schmidt, T. Single-Molecule Imaging of the H-Ras Membrane-Anchor Reveals Domains in the Cytoplasmic Leaflet of the Cell Membrane. *Biophys. J.* **2004**, *86* (1), 609−616.

(33) Kusumi, A.; Sako, Y.; Yamamoto, M. Confined lateral diffusion of membrane receptors as studied by single particle tracking (nanovid microscopy). Effects of calcium-induced differentiation in cultured epithelial cells. *Biophys. J.* **1993**, *65* (5), 2021−2040.

(34) Blanco, M.; Walter, N. G. In *Methods in Enzymology*; Nils, G. W., Ed.; Academic Press: 2010; Vol. *472*, Chapter 9, pp 153−178.

(35) Han, B.; Li, C.; Zhang, C.; Li, C. Research on Properties of EB/EVA Semiconductive Shielding Composites. *Adv. Mater. Res.* **2014**, *989−994*, 629−633.

(36) Chen, X. L.; Cui, P.; Ji, Y. P. Rheological and E.ectrical Properties of CB/HDPE Composites. *Appl. Mech. Mater.* **2013**, *333−335*, 1872−1875.

(37) Sharma, S.; Volosin, A. M.; Schmitt, D.; Seo, D.-K. Preparation and electrochemical properties of nanoporous transparent antimony-doped tin oxide (ATO) coatings. *J. Mater. Chem. A* **2013**, *1* (3), 699−706.

(38) Correa Baena, J. P.; Agrios, A. G. Transparent Conducting Aerogels of Antimony-Doped Tin Oxide. *ACS Appl. Mater. Interfaces* **2014**, *6* (21), 19127−19134.

DOI: 10.1021/acs.langmuir.7b00761
Langmuir 2017, 33, 6410−6418

(39) Baena, J. P. C.; Agrios, A. G. Antimony-Doped Tin Oxide Aerogels as Porous Electron Collectors for Dye-Sensitized Solar Cells. *J. Phys. Chem. C* **2014**, *118*, 17028−17035.
(40) Wang, Y.; Brezesinski, T.; Antonietti, M.; Smarsly, B. Ordered Mesoporous Sb-, Nb-, and Ta-Doped SnO_2 Thin Films with Adjustable Doping Levels and High Electrical Conductivity. *ACS Nano* **2009**, *3* (6), 1373−1378.
(41) Volosin, A. M.; Sharma, S.; Traverse, C.; Newman, N.; Seo, D.-K. One-pot synthesis of highly mesoporous antimony-doped tin oxide from interpenetrating inorganic/organic networks. *J. Mater. Chem.* **2011**, *21* (35), 13232−13240.
(42) Alothman, Z. A Review: Fundamental Aspects of Silicate Mesoporous Materials. *Materials* **2012**, *5* (12), 2874−2902.
(43) Mayagoitia, V. The Five Types of Porous Structures and Their Hysteresis Loops. *Stud. Surf. Sci. Catal.* **1991**, *62*, 51−60.
(44) Liu, M.; Fu, J.; Hejesen, C.; Yang, Y.; Woodbury, N. W.; Gothelf, K.; Liu, Y.; Yan, H. A DNA tweezer-actuated enzyme nanoreactor. *Nat. Commun.* **2013**, *4*, 2127.
(45) Aguzzi, A.; O'Connor, T. Protein aggregation diseases: pathogenicity and therapeutic perspectives. *Nat. Rev. Drug Discovery* **2010**, *9* (3), 237−248.
(46) Siddhanta, S.; Barman, I.; Narayana, C. Revealing the trehalose mediated inhibition of protein aggregation through lysozyme-silver nanoparticle interaction. *Soft Matter* **2015**, *11* (37), 7241−7249.
(47) Pitchiaya, S.; Androsavich, J. R.; Walter, N. G. Intracellular single molecule microscopy reveals two kinetically distinct pathways for microRNA assembly. *EMBO Rep.* **2012**, *13* (8), 709−715.

DOI: 10.1021/acs.langmuir.7b00761
Langmuir 2017, 33, 6410−6418

Supporting Information

Tracking Single DNA Nanodevices in Hierarchically Meso-Macroporous Antimony-Doped Tin Oxide Demonstrates Finite Confinement

Daniel Mieritz,[†‖] Xiang Li,[‡‖] Alex Volosin,[†] Minghui Liu,[†,§] Hao Yan,[†,§] Nils G. Walter,[*,‡] and Dong-Kyun Seo[*,†]

Correspondence: nwalter@umich.edu, dseo@asu.edu

Contents:

SUPPLEMENTAL FIGURES

Characterizations of ATO Coatings by SEM and TEM

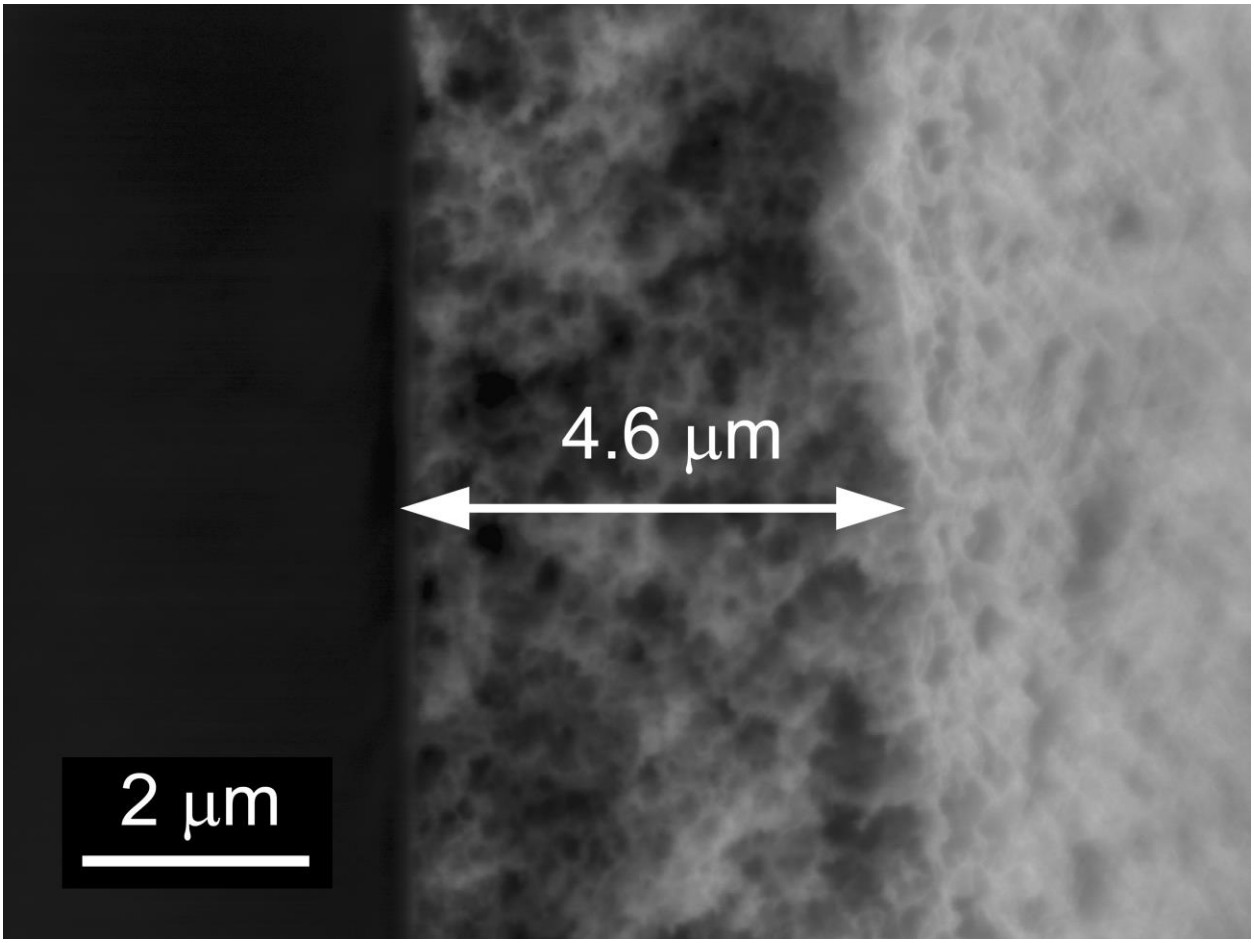

Figure S1. Edge-on SEM image of meso-macroporous ATO coating, where the thickness is measured to be 4.6 μm (scale bar = 2 μm).

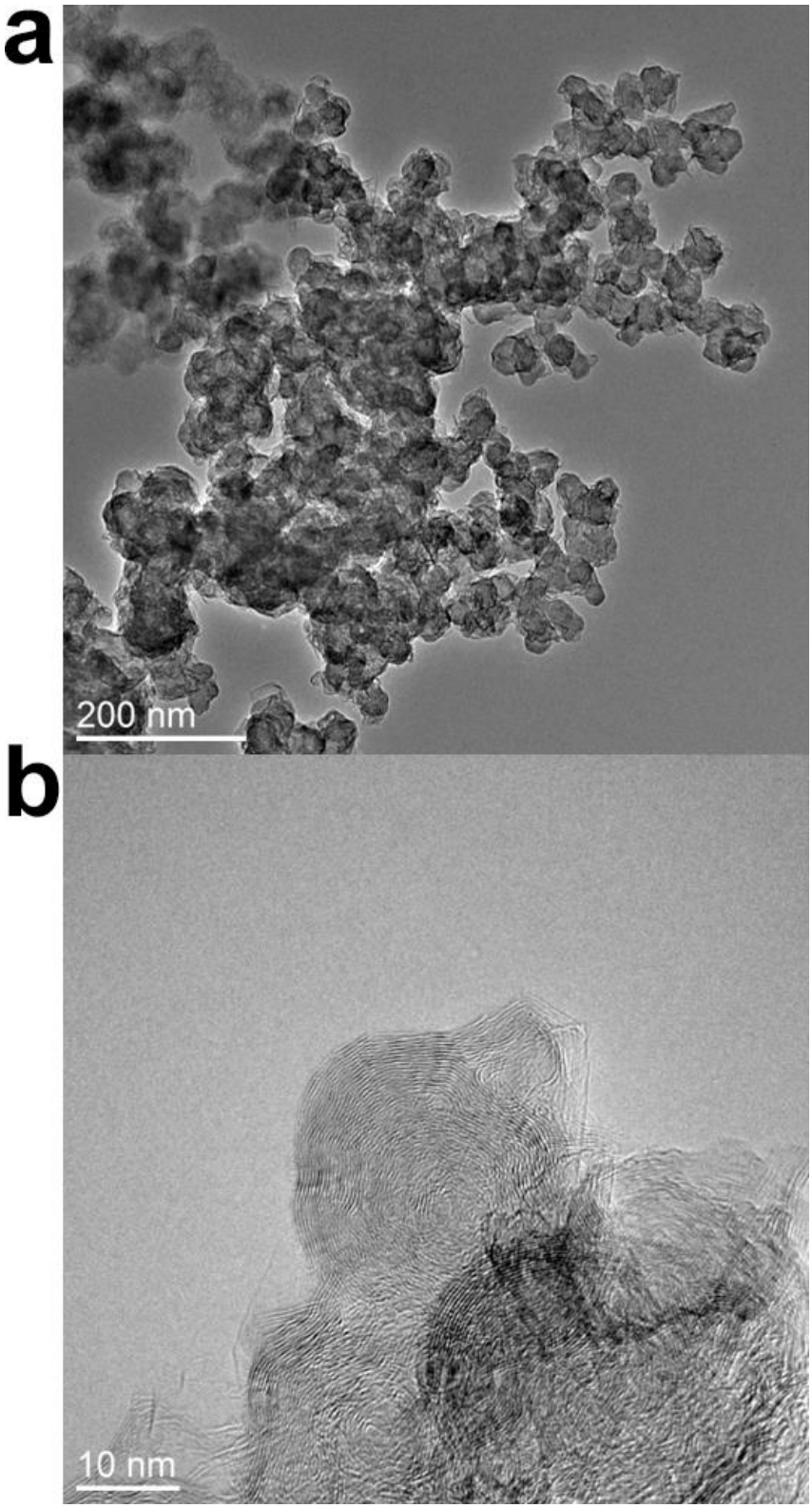

Figure S2. TEM micrographs of the carbon black template. The scale bars are 200 nm (a) and 10 nm (b).

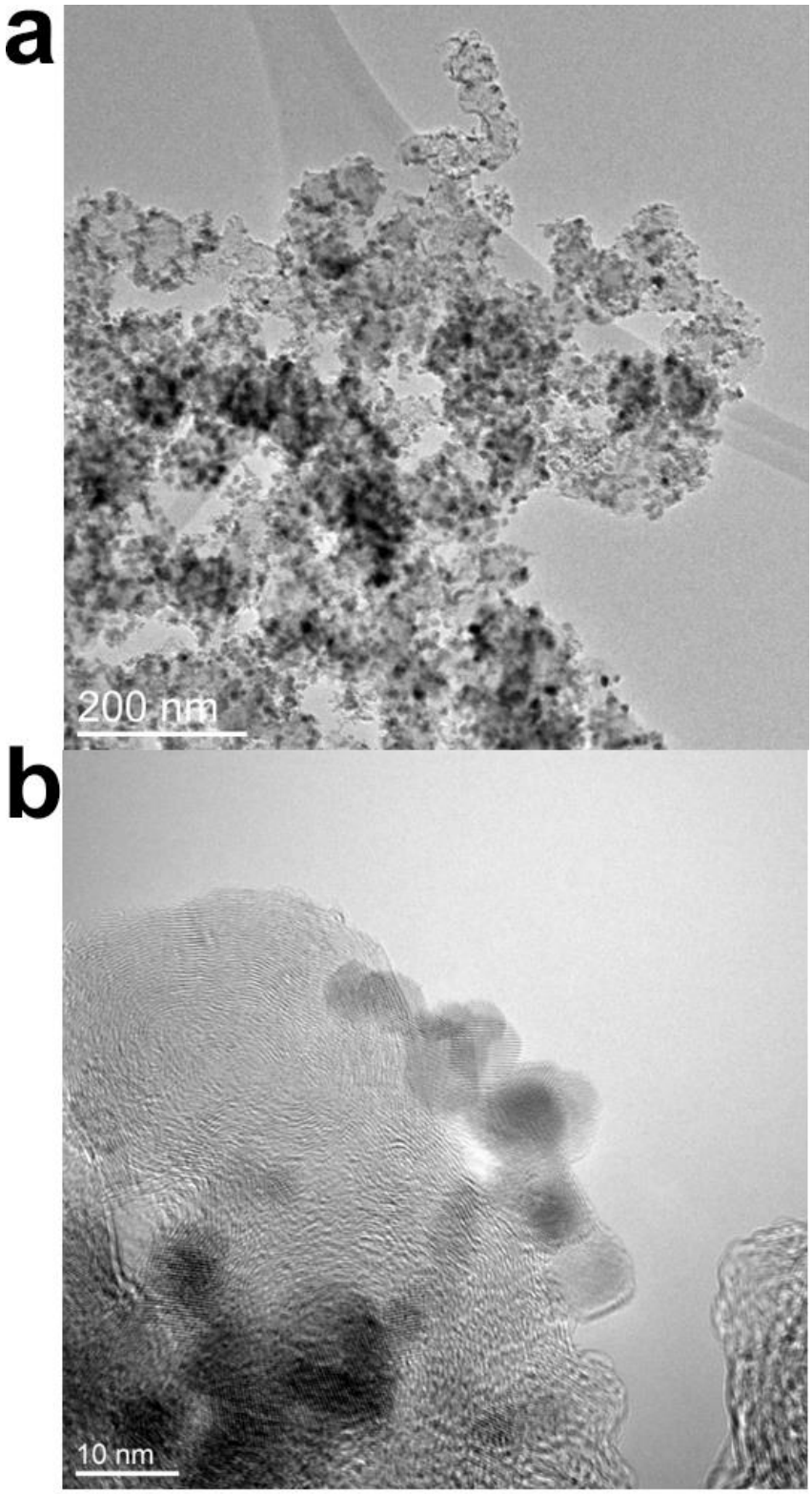

Figure S3. TEM micrographs of the pyrolyzed reaction mixture. The scale bars are 200 nm (a) and 10 nm (b).

Single molecule microscopy data

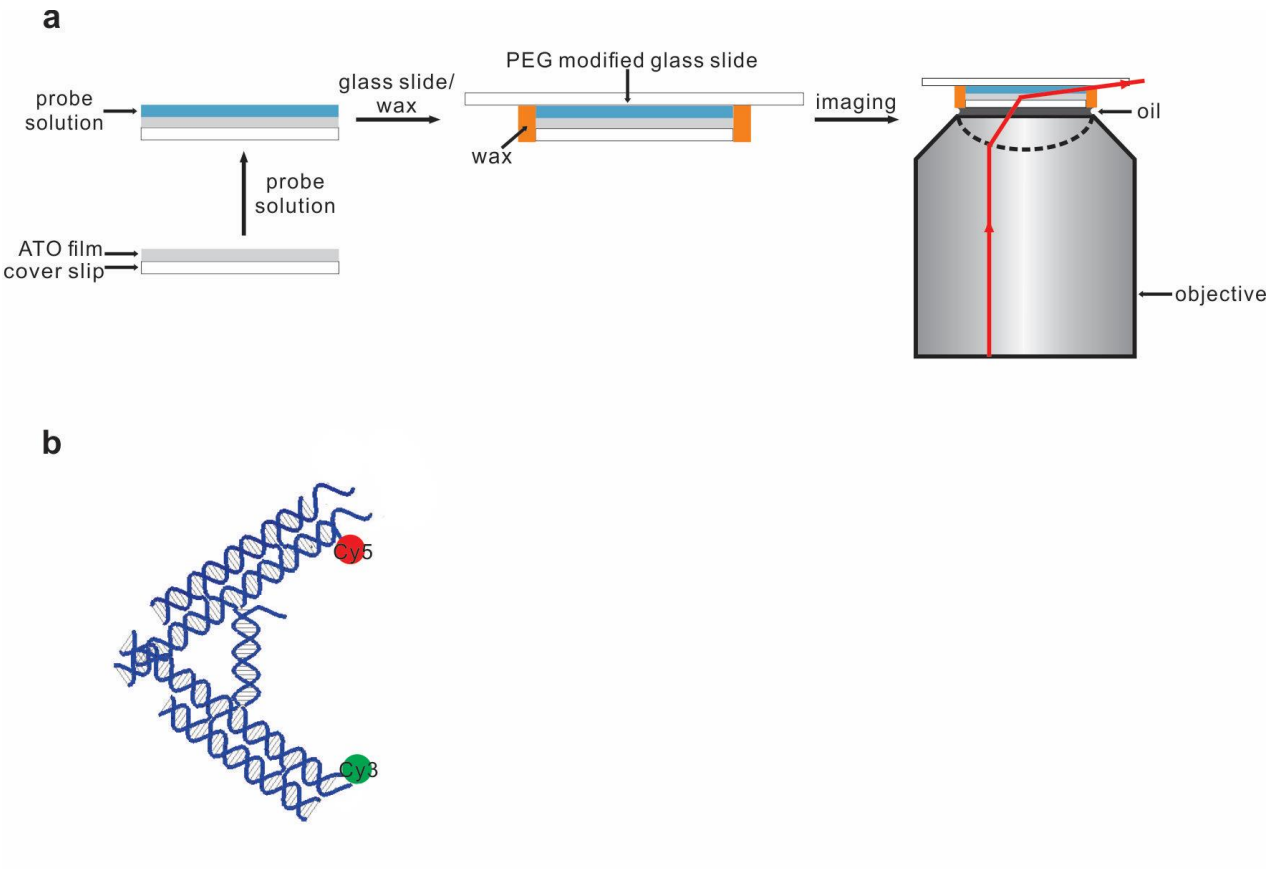

Figure S4. Characterization of our meso-macroporous ATO coatings with fluorescently labeled DNA nanotweezer probes by single particle tracking. (a) Experimental design for sample preparation and imaging. The structural details of the DNA nanotweezer are shown in (b) with the Cy3 and Cy5 fluorophore labeling sites indicated.

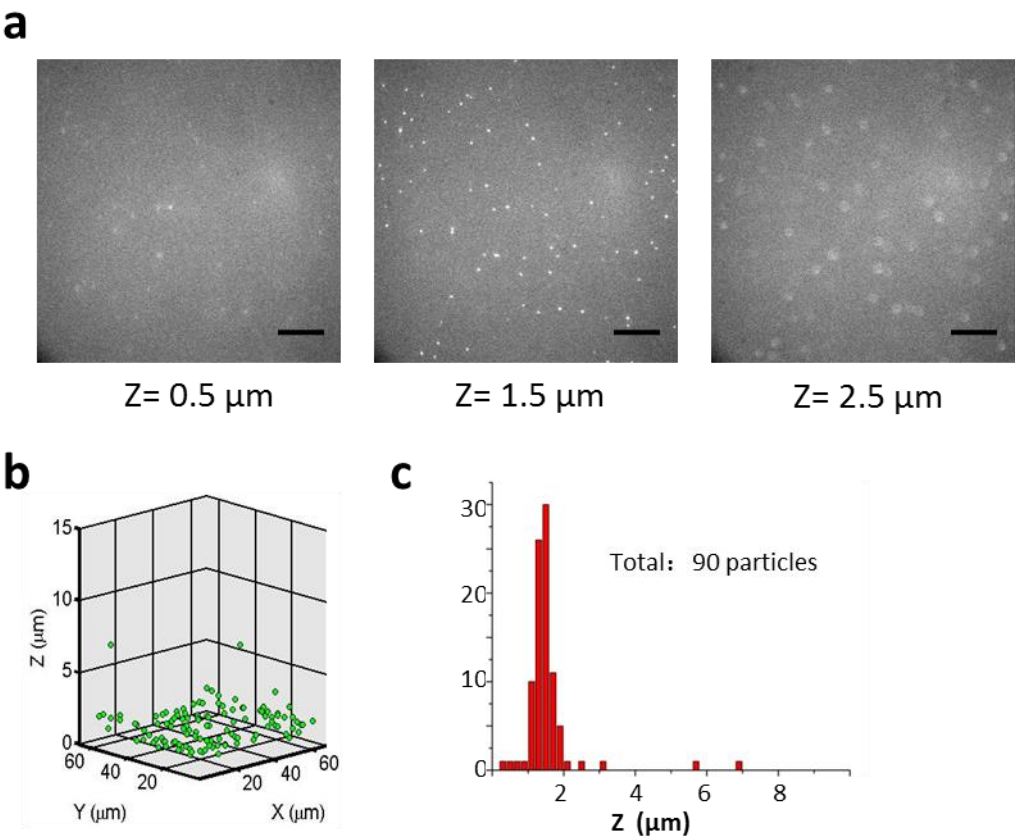

Figure S5. Distribution of DNA nanotweezers along the z-axis when directly deposited onto the glass surface. (a) Raw images of DNA tweezers at different focal planes. The 3D and z-axis distributions are summarized in (b) and (c). Scale bar = 5 µm.

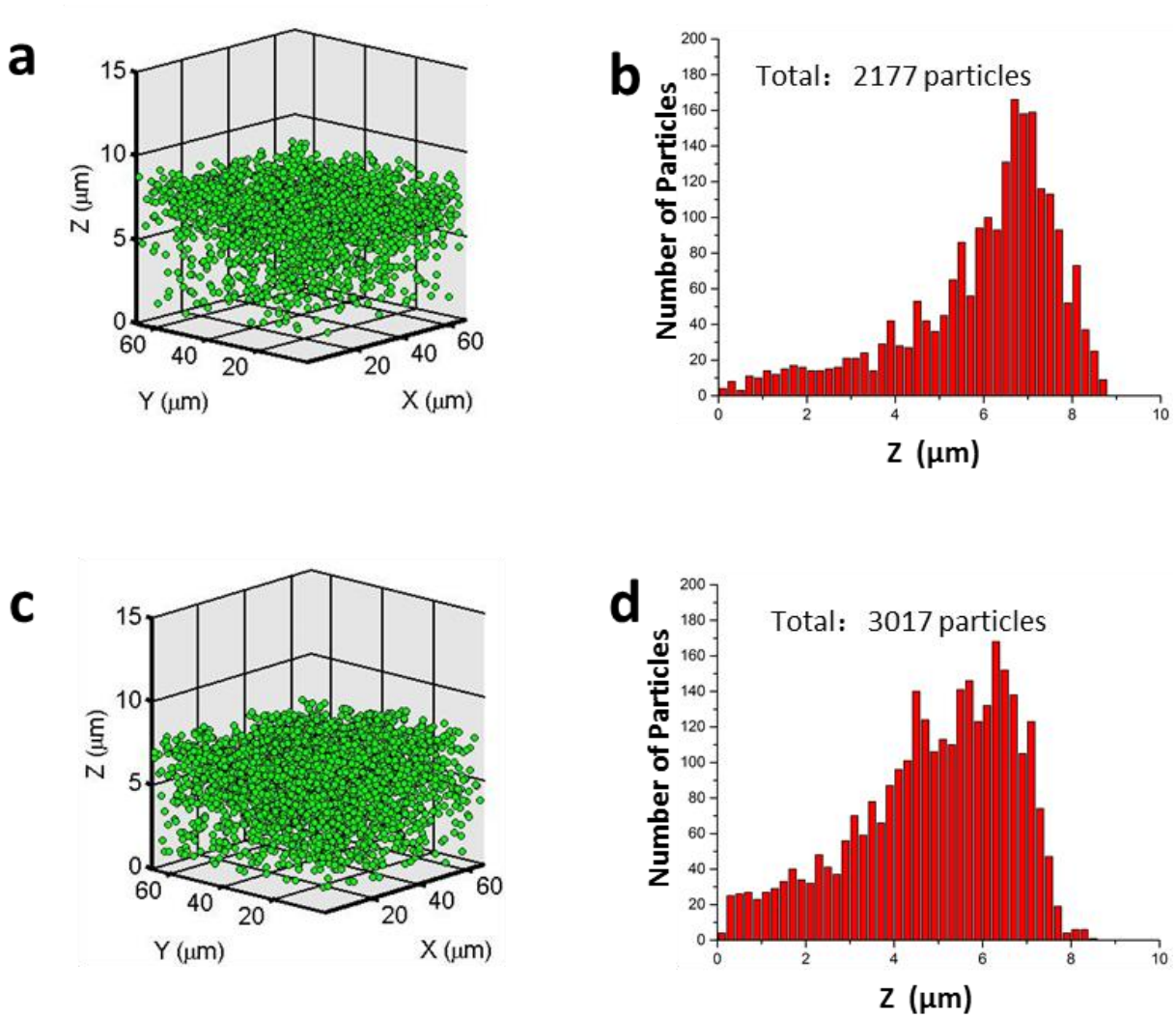

Figure S6. Distribution of DNA nanotweezers along the z-axis inside our meso-macroporous ATO coating at varying Mg^{2+} concentrations. The 3D distribution is summarized in (a) and (b) for 10 m*M* $MgCl_2$, and in (c) and (d) for 100 m*M* $MgCl_2$.

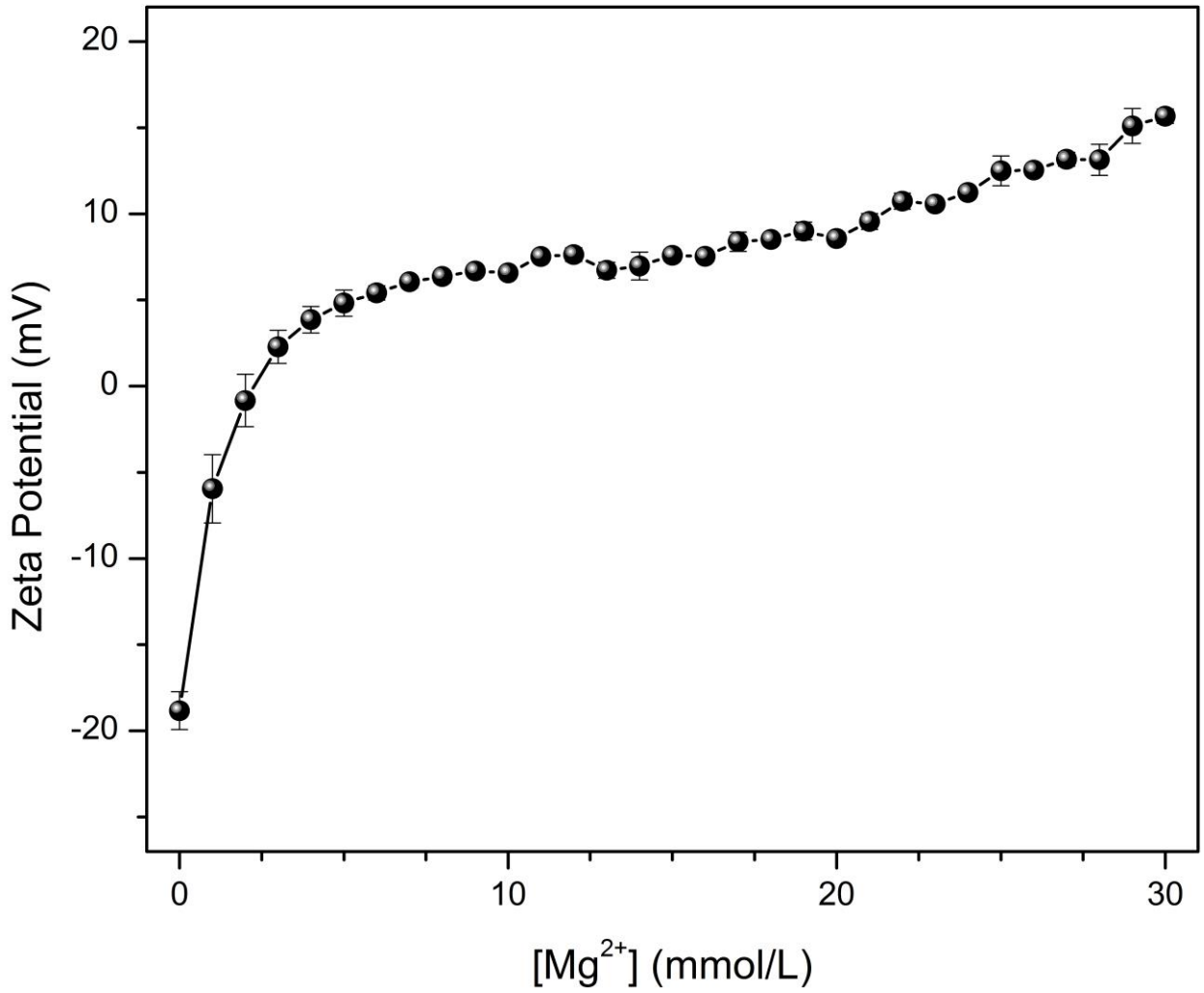

Figure S7. Zeta potential of our meso-macroporous ATO coating measured at varying Mg^{2+} concentrations.

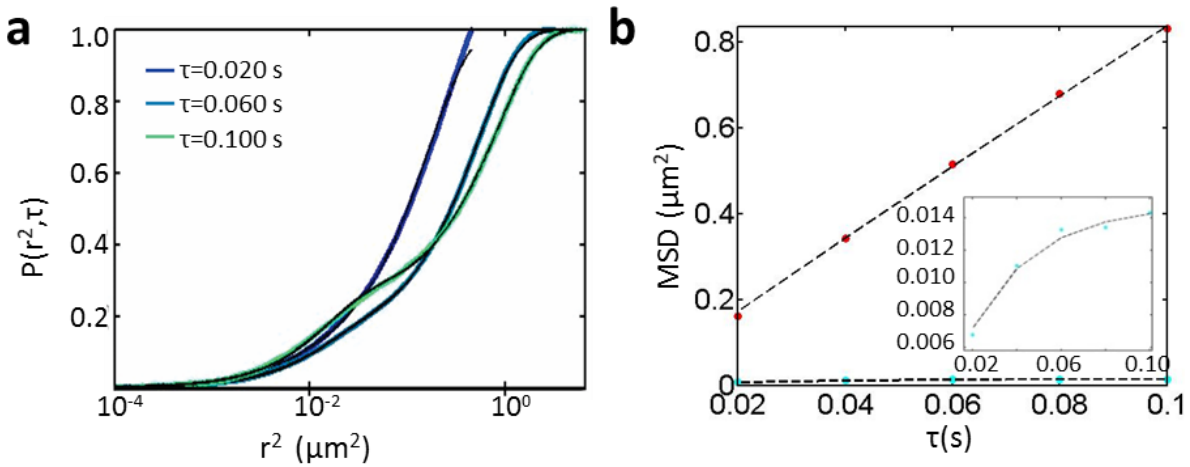

Figure S8. (a) Fitting curves of squared step sizes (r^2) of DNA probes with the 2-term 2D CPD function at three different τ values (fitting as described in Materials and Methods). Three colored lines (corresponding to three different τ) are the calculated statistic analyses from the trajectory data and the black lines are the fittings which overall overlap with the color lines. (b) MSD versus τ for the fast (red) and slow (green) subpopulations of DNA probes obtained from the 2-term CPD fitting. An inset of the zoomed result of the slow subpopulation is also provided.

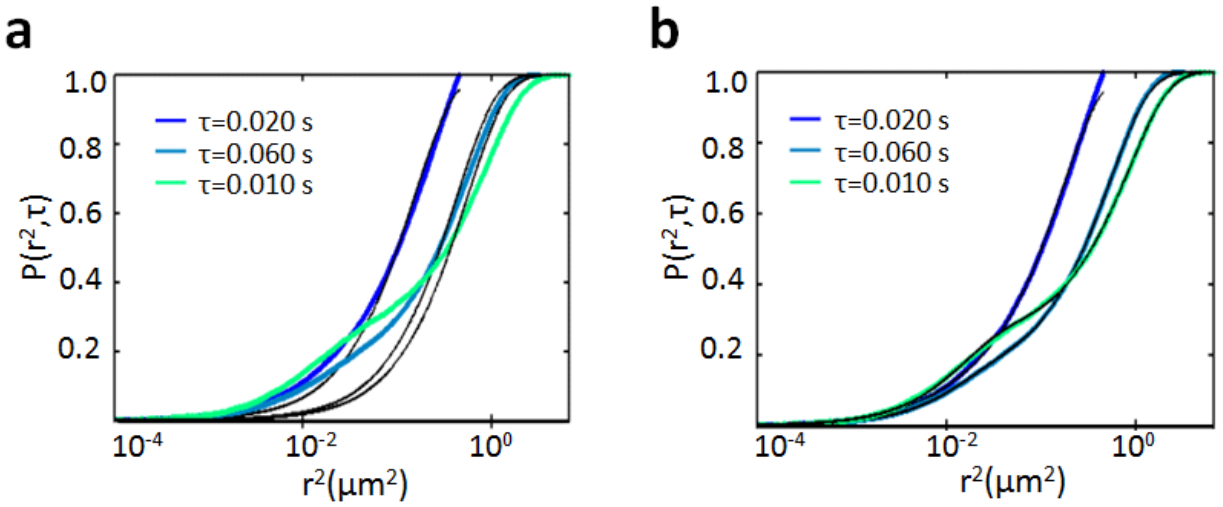

Figure S9. 2D CPD function fitting of squared step sizes of DNA probes fitted with 1-term (a) and 3-term (b) functions. Three colored lines in each plot are the statistic analysis from the trajectory data and the black lines are the fitting result. Obviously, the 1-term fitting is not sufficient and with large errors, as shown in (a). Comparing to 1-term fitting, the 2-term (Figure S8) and 3-term fittings are significantly improved with much smaller errors. For the 3-term fitting, two of the three subpopulations are almost identical, indicating that they should be in the same group and that there are overall two major subpopulations for the DNA probes.

SUPPLEMENTAL EXPERIMENTAL PROCEDURES

Fabrication of hierarchically porous coatings

The synthesis of hierarchically porous ATO was carried out by a previously reported sol-gel route for producing meso-macroporous coatings. Preparation of coatings of the hierarchically porous ATO were prepared in the same fashion as the reference from the main text, but on cover glass (VWR, No. 1.5, 22 × 22 mm) instead. Two sets of control experiments were carried out in parallel. To study the morphology of the carbon black and PEG template, the synthesis was carried out without the metal salts, and a coating was prepared in the same fashion. For morphological understanding of the templating effect of carbon black, the coating was pyrolyzed under an Ar atmosphere in the same heating procedure.

Characterizations of structure, morphology and surface properties

Powder X-ray diffraction (PXRD) was performed on a Siemens D5000 diffractometer using Cu Kα radiation. Five coatings were scraped from the cover glass substrates, and were crushed well with a small amount of silicon powder as internal standard (a = 5.4301 Å); the resulting mixture was dispersed in ethanol and spread on a quartz plate. Data were acquired by scanning the 2θ angle from 5 to 90° with a step size of ~ 0.016° and a scan time of two hours. The (111) Si reflection at 2θ = 28.443° was used as a reference during unit cell analysis, which was carried out using PANalytical X'Pert Pro Software. Stylus profilometry was carried out using a Dektak XT with a 12.5 µm diameter tip and two mg of force. The profile was obtained with a line scan across the ATO coating, beginning and ending on the cover class substrate. Optical profilometry was conducted with a ZeScope, using an objective lens. The ZeMap software was used to analyze a linear portion of the 3D map.

Nitrogen sorption isotherms were obtained from the bulk powder using a Micromeritics ASAP 2020 Surface Area and Porosity Analyzer at 77 K. The powder was degassed under vacuum at 250 °C for 8 hours before data collection. The Brunauer–Emmett–Teller (BET) model was applied to the adsorption branch in the partial pressure range of 0.05 – 0.2. Pore size distribution was analyzed using the Barrett–Joyner–Halenda model applied to the desorption branch, with the Halsey thickness curve for non-uniform surfaces and the Faas-correction for multilayer desorption.[1] Total pore volume was estimated from the quantity of gas adsorbed at p/p_0 ~ 0.99. The zeta potential of samples dispersed in buffer solutions through 20 min of sonication was measured with a Malvern Zetasizer Nano. Subsequently, these dispersions were auto-titrated against a 0.50 *M* solution of $MgCl_2$ using the MPT-2 accessory, in increments of 1 m*M*, and the zeta potential was measured in triplicate between each addition. Data were collected using the Malvern software.

Scanning electron microscopy (SEM) studies were conducted on ATO coatings on cover glass substrates and contacted by carbon tape, with an FEI XL-30 Environmental SEM using 20 keV electrons. Transmission electron microscopy (TEM) was performed on the scraped ATO coating that was crushed lightly and dusted onto the TEM grid. For high-resolution TEM (HR-TEM) studies, the scraped ATO coating was sonicated in ethanol for 20 min, and the TEM grid was immediately immersed in the dispersion and air-dried. Images of carbon black were obtained by gently dusting the carbon black reagent onto a TEM grid. Micrographs were obtained on a JEOL 2010F at an accelerating voltage of 200 kV.

Details of SPT Studies

The design and preparation of the DNA nanotweezers (Figure S4b) at a concentration of 5 n*M* followed previously described protocols (see text for references). SPT was performed on an Olympus IX-81 objective-type total internal reflection fluorescence (TIRF) microscope using a 1.40NA oil-immersion objective in HILO imaging mode for low-background data acquisition at varying sample depths.[2] Fluorescence was detected on a 512 pixel × 512 pixel EMCCD (Evolve 512, Photometrics) camera under 640 nm illumination (using a Coherent CUBE 640-100 laser) and employing a 660 nm edge BrightLine® single-edge dichroic beamsplitter.

SUPPLEMENTAL REFERENCES

(1) Halsey, G., Physical Adsorption on Non-Uniform Surfaces. *J. Chem. Phys.* **1948,** *16* (10), 931-938.

(2) Pitchiaya, S.; Krishnan, V.; Custer, T. C.; Walter, N. G., Dissecting non-coding RNA mechanisms in cellulo by Single-molecule High-Resolution Localization and Counting. *Methods* **2013,** *63* (2), 188-199.